

DOI: 10.1002/ ((please add manuscript number))

Article type: Full Paper

Multi-scale Investigations of δ -Ni_{0.25}V₂O₅·nH₂O Cathode Materials in Aqueous Zinc-ion Batteries

Jianwei Li^a, Kit McColl^a, Xuekun Lu^b, Sanjayan Sathasivam^a, Haobo Dong^a, Liqun Kang^b, Zhuangnan Li^a, Siyu Zhao^a, Andreas G. Kafizas^d, Ryan Wang^b, Dan J. L. Brett^b, Paul R. Shearing^b, Furio Corà^a, Guanjie He^{*a, b, c}, Claire J. Carmalt^a and Ivan P. Parkin^{a*}

Mr. Jianwei Li, Dr. Kit McColl, Dr. Sanjayan Sathasivam, Mr. Haobo Dong, Dr. Zhuangnan Li, Mr. Siyu Zhao, Prof. Furio Corà, Dr. Guanjie He, Prof. Claire J. Carmalt and Prof. Ivan P. Parkin

^aChristopher Ingold Laboratory, Department of Chemistry, University College London, 20 Gordon Street, London WC1H 0AJ, U.K. Email: g.he@ucl.ac.uk; i.p.parkin@ucl.ac.uk

Dr. Xuekun Lu, Mr. Liqun Kang, Dr. Ryan Wang, Prof. Dan J. L. Brett, Paul R. Shearing^b,

^bElectrochemical Innovation Lab, Department of Chemical Engineering, University College London, London WC1E 7JE, U.K.

Dr. Guanjie He

^cSchool of Chemistry, University of Lincoln, Joseph Banks Laboratories, Green Lane, Lincoln, LN6 7DL, U.K.

^dThe Grantham Institute, Imperial College London, London, SW7 2AZ, U.K.

Keywords: Zn-ion battery, cathode, DFT calculation, 3D tomography

Abstract

Cost-effective and environmentally friendly aqueous zinc-ion batteries (AZIB) exhibit tremendous potential for application in grid-scale energy storage systems but are limited by suitable cathode materials. Hydrated vanadium bronzes have gained significant attention for AZIBs and can be produced with a range of different pre-intercalated ions, allowing their properties to be optimised. However, gaining a detailed understanding of the energy storage mechanisms within these cathode materials remains a great challenge due to their complex crystallographic frameworks, limiting rational design from the perspective of enhanced Zn²⁺

diffusion over multiple length scales. Herein, we report on a new class of hydrated porous δ - $\text{Ni}_{0.25}\text{V}_2\text{O}_5 \cdot n\text{H}_2\text{O}$ nanoribbons for use as an AZIB cathode. The cathode delivers reversibility showing 402 mAh g^{-1} at 0.2 A g^{-1} and a capacity retention of 98 % over 1200 cycles at 5 A g^{-1} . A detailed investigation using experimental and computational approaches reveal that the host ‘ δ ’ vanadate lattice has favourable Zn^{2+} diffusion properties, arising from the atomic-level structure of the well-defined lattice channels. Furthermore, the microstructure of the as-prepared cathodes is examined using multi-length scale X-ray computed tomography for the first time in AZIBs and the effective diffusion coefficient is obtained by image-based modelling, illustrating favourable porosity and satisfactory tortuosity.

1. Introduction

There has been rapid development of new and renewable energy harvesting devices that draw power from sunlight and wind. These devices require low-cost and reliable energy storage devices to allow energy release at night and for continuous supply under low wind conditions. The most prevalent type of secondary energy storage uses lithium-ion batteries (LIBs), that possess high energy density and long cycle life and have brought about a remarkable technical revolution for portable electronics, vehicles and many other aspects in daily life.^[1] However, considering the growing cost of the limited lithium resources and safety concerns derived from intrinsic chemical activity of metallic lithium and its combustible ester electrolytes, aqueous rechargeable batteries have been recently spotlighted as promising alternatives especially for utilisation of large-scale energy storage stations.^[2] Among them, zinc-ion batteries (ZIBs) have gained exceptional interest in aqueous systems due to the beneficial physicochemical properties of zinc, that is, i) a high theoretical volumetric capacity around 5585 mAh cm^{-3} of a metallic zinc anode compared with 2061 mAh cm^{-3} and 1129 mAh cm^{-3} for lithium and sodium anodes, respectively; ii) low redox potential of -0.762 V vs. standard hydrogen electrode and iii) electrochemical stability of metallic zinc in its sulfate solutions at

near neutral or slightly acidic aqueous electrolyte providing the batteries with safe, cost-effective and environmentally-friendly characteristics.^[3,4,5,6]

Owing to the attractive properties of AZIBs, many efforts have been devoted to the investigation of cathode materials such as Prussian blue analogs,^[7,8] manganese-based oxides,^[9,10] vanadium-based oxides⁵ and organic compounds.^[11,12] Despite Zn^{2+} ions having a relatively small ionic radius (0.74 Å) and relatively high ionic conductivities in aqueous electrolytes (*ca.* 1–10 mS cm⁻¹),¹³ achieving reversible insertion into cathode hosts with high capacity and long cycle life remains a challenge because of the much stronger electrostatic interaction of divalent Zn^{2+} ions with the cathode material framework compared with that of Li^+ ions, and the difficulties of co-intercalation of the larger hydrated Zn^{2+} complexes (4.3 Å for hydration ion radius of Zn^{2+}).^[14,15] Layered vanadium bronzes are considered promising candidates for AZIB cathode applications owing to the relatively facile reversible chemical valence of vanadium between 3+ and 5+ oxidation states, offering high specific capacity (> 300 mAh g⁻¹) and expandable interlayer spacing upon charge/discharge of Zn^{2+} ions.^[16,17] Moreover, the layered V_2O_5 host structure is compositionally flexible and allows pre-intercalated guest species from metal ions to water to organic molecules to be accommodated within the interlayer space. This allows properties such as cycle life, ion diffusion and inherent conductivity to be tuned by the choice of interlayer guest species. Modifications of behaviour have been understood in terms of a charge screening effects between the divalent Zn^{2+} and the cathode by water molecules, structure stabilizing “pillars” arising from guest species, and shallow donor levels due to reduced framework V ions.^[18,19,20] Although many pre-intercalated metal ions in V_2O_5 hosts have been investigated, such as $\text{Zn}_{0.25}\text{V}_2\text{O}_5$,^[17] $\text{Mg}_{0.34}\text{V}_2\text{O}_5$,^[16] $\text{Ca}_{0.25}\text{V}_2\text{O}_5$,^[21] $\text{Na}_{0.33}\text{V}_2\text{O}_5$,^[19] $\text{Mn}_x\text{V}_2\text{O}_5$,^[22] and $\text{Cu}_x\text{V}_2\text{O}_5$,^[23] the crystallographic complexity of the double-layer V_2O_5 host lattice and challenges associated with evaluating the precise role of different various pre-intercalated ions has limited systematic improvements in the design of these cathode materials. In addition, there is limited

discussion in previous literature in regards to the nature of the layers within the host V_2O_5 framework, which can be classified as either a δ - or σ -type, yet which display different vanadium coordination polyhedra and incorporate different guest ions.^[24,25,26,27,28] To further improve Zn^{2+} ion insertion/desertion behaviour, inducing porous and hollow structures have been demonstrated as effective approaches.^[29,30] However, most of the synthetic methods reported to date are template-assisted, which are time-consuming and involve multi-steps.^[31,32]

In this work, we report self-templated porous hydrated δ - $Ni_{0.25}V_2O_5$ nanoribbons as cathode materials for AZIBs from a single-step hydrothermal process. The materials exhibit excellent, best in class, specific capacity (402 mAh g^{-1} at 0.2 A g^{-1}) and extraordinary cycling stability (98 % retention of 214 mAh g^{-1} at 5 A g^{-1} after 1200 cycles). A similar synthetic process was used to prepare isomorphous hydrated δ - $Co_{0.25}V_2O_5$. To the best of our knowledge, it is the first time that these two crystallographic phase materials have been utilised in battery applications, and their differing electrochemical behaviours were elucidated in detail *via ex-situ* Raman, *ex-situ* near edge X-ray absorption fine structure (NEXAFS) and *ex-situ* energy dispersive spectroscopy (EDS) elemental analysis. The results give new insight into the role of different pre-intercalated ions in the hydrated V_2O_5 framework. The mechanism of Zn-ion storage in $Ni_{0.25}V_2O_5 \cdot nH_2O$ was investigated through a combined experimental and computational approach, providing insight into how the atomic-level properties of the cathode affect overall electrochemical performance. Furthermore, design strategies for these materials to improve Zn-ion diffusion behaviour over large electrode length-scales were unravelled *via* state-of-the-art X-ray tomography and simulation techniques.

2. Results and Discussion

The synthetic process to fabricate hydrated $Ni_{0.25}V_2O_5 \cdot nH_2O$ and $Co_{0.25}V_2O_5 \cdot nH_2O$ nanoribbons was carried out by a single-step hydrothermal method (see details in Supporting

Information). Notably, both materials were bronze in colour (Figure S1). As depicted in Figure 1a, a highly porous $\text{Ni}_{0.25}\text{V}_2\text{O}_5 \cdot n\text{H}_2\text{O}$ nanoribbon was observed by transmission electron microscopy (TEM) and scanning tunnelling electron microscopy (STEM) (Figure S2a, b) with a typical size of over 10 μm in length and hundreds of nanometres in width, which could be attributed to acetate ligands in system steadily binding to the metal ions in a bidentate or bridging fashion for continuous control of self-assembly growth.^[33] The coupling of metal-acetate occurs at high pressure and high temperature, forming organized porous micro-structures. Additionally, the N_2 adsorption-desorption measurement (at 77K) was adopted to elucidate the specific surface area and pore size distribution of as-obtained $\delta\text{-Ni}_{0.25}\text{V}_2\text{O}_5 \cdot n\text{H}_2\text{O}$ powder (Fig. S1 b, c). Specifically, the results showed a Brunauer-Emmett-Teller (BET) specific surface area of $25.8 \text{ m}^2 \text{ g}^{-1}$ and abundant pores with a diameter of $\sim 5 \text{ nm}$ according to Barrett-Joyner-Halenda (BJH) method analysis, which is consistent with observation from HRTEM as mentioned above. Scanning electron microscopy (SEM) and EDS characterization (Figure S2c, d) were used to clarify the ordered geometric morphology of the material, and the uniform distribution of Ni and V elements with an elemental ratio of V to Ni around 8.8:1. The X-ray diffraction (XRD) pattern of the as-prepared materials (Figure 1b) can be indexed to monoclinic $\text{Ni}_{0.22}\text{V}_2\text{O}_5$ in C_2/m space group, with lattice parameters determined by Rietveld refinement of $a = 11.756(3) \text{ \AA}$, $b = 3.649(1) \text{ \AA}$, $c = 10.364(5) \text{ \AA}$, $\alpha = \gamma = 90^\circ$ and $\beta = 95.03(4)^\circ$, $V = 442.88(6) \text{ \AA}^3$ (JCPDS No. 88-0580), which is consistent with previous reports of $\delta\text{-}[\text{Ni}(\text{H}_2\text{O})_4]_{0.25}\text{V}_2\text{O}_5$.^[24, 34] In the $\text{Ni}_{0.25}\text{V}_2\text{O}_5$ pattern, the dominant intensity of (001) peak at 2θ of $\sim 3.94^\circ$ corresponds to an interlayer spacing of 10.3 \AA , and the peaks at 11.67° and 11.85° refer to the (110) and (003) planes respectively. In addition, the XRD Rietveld refinement of $\delta\text{-Ni}_{0.25}\text{V}_2\text{O}_5 \cdot n\text{H}_2\text{O}$ and corresponding results of lattice parameters are presented in Figure S2e and Table S1. Similarly, $\text{Co}_{0.25}\text{V}_2\text{O}_5$ materials show the same nanoribbon structures (Figure S3a, b) and the XRD plot of as-prepared $\text{Co}_{0.25}\text{V}_2\text{O}_5$ materials can also be well-matched with standard pattern of $\text{Ni}_{0.25}\text{V}_2\text{O}_5$ (Figure

S3c). A slight shift of peaks to lower 2θ values in $\text{Co}_{0.25}\text{V}_2\text{O}_5 \cdot n\text{H}_2\text{O}$, compared with the $\text{Ni}_{0.25}\text{V}_2\text{O}_5 \cdot n\text{H}_2\text{O}$ pattern, can be interpreted as a larger hydrated radius of hexa-aqua Co^{2+} complexes (4.23 Å) than Ni^{2+} (4.04 Å). The crystal structure of $\text{Ni}_{0.25}\text{V}_2\text{O}_5 \cdot n\text{H}_2\text{O}$ was further confirmed by HRTEM showing the lattice space of 0.186 and 0.217 nm, which can be indexed to (404) and ($\bar{3}13$) planes of $\text{Ni}_{0.25}\text{V}_2\text{O}_5 \cdot n\text{H}_2\text{O}$ (Figure 1c) respectively, and thus is in accordance with XRD results. It should be emphasized that the $\text{Ni}_{0.25}\text{V}_2\text{O}_5 \cdot n\text{H}_2\text{O}$ materials (Figure 1d) possess a distinctly different atomic level structure to previously reported hydrated ‘double-layer’ $\delta\text{-Ca}_{0.24}\text{V}_2\text{O}_5 \cdot n\text{H}_2\text{O}$ ^[21] (Figure 1e), $\sigma\text{-Zn}_{0.25}\text{V}_2\text{O}_5 \cdot n\text{H}_2\text{O}$ ^[17] and $\sigma\text{-Mg}_{0.34}\text{V}_2\text{O}_5 \cdot n\text{H}_2\text{O}$ ^[16] phases (Figure 1f, S4). In the $\sigma\text{-M}_x\text{V}_2\text{O}_5 \cdot n\text{H}_2\text{O}$ ($M = \text{Zn}^{2+}, \text{Mg}^{2+}$) structures, the individual V_2O_5 layers forming the ‘double-layer’ structure contain 4, 5 and 6 coordinated V ions. In the $\delta\text{-M}_x\text{V}_2\text{O}_5 \cdot n\text{H}_2\text{O}$ structures ($M = \text{Ni}^{2+}, \text{Co}^{2+}$ and Ca^{2+}), the individual layers in the ‘double-layer’ motif have the same structure as layers in $\alpha\text{-V}_2\text{O}_5$ and contain 5 and 6-coordinated V ions only. Furthermore, the large Ca^{2+} ions in the δ -phase coordinate to three apical O-ions in the V_2O_5 layers; one in one layer and two in the adjacent layer (Figure 1e), whereas Ni^{2+} ions coordinate to only two O ions through axial Ni-O bonds (Figure 1d & S4a). Thus, in the Ni-intercalated δ -phase, there are a higher number of apical O-ions in the V_2O_5 layer available for Zn^{2+} ions to coordinate upon intercalation than in the Ca δ -phase. Both the σ - and δ -structure of the ‘double-layer’ motif, and the nature of the intercalated ions in the δ -phase are expected to have a strong influence on the Zn^{2+} ion intercalation properties, since the local coordination environment experienced by the Zn^{2+} ion in the structure will be different in each case. The Raman spectrum of $\text{Ni}_{0.25}\text{V}_2\text{O}_5 \cdot n\text{H}_2\text{O}$ in Figure 1g exhibits seven main peaks in the range of 100-1200 cm^{-1} which can be assigned to different vibrational modes in terms of motions of V_2O_5 units, V-O-V bending and V=O and V-O stretching modes.^[35,36,37] Specifically, low-frequency modes of 104 and 175 cm^{-1} can be interpreted to a translational mode originated from relative motions of double layer sheet

belonging to unit cells, *i.e.* stretching vibrations of particular vanadyl bonds in VO₆ octahedra.^[38] The strongest signal of 175 cm⁻¹ reflects a long-range order associated with the in-plane *ab* direction of the V₂O₅ sheets.³⁹ The band at 965 cm⁻¹ refers to the stretching mode of the terminal apical V=O which presents at a slightly lower wavelength compared to α -V₂O₅ (994 cm⁻¹).^[40] This observation can be interpreted as a lengthening of the V=O vanadyl bond due to Ni²⁺ accommodation into the interplanar space. The Ni²⁺ coordinates with the apical O in the double sheet layer, resulting in a linear expansion of the interlayer spacing of the lattice, which is consistent with the observation that lithium intercalated V₂O₅ exhibited a similar shift in the frequency from 994 to 984 cm⁻¹ upon the progressive addition of lithium in α -V₂O₅.^[41] A Raman shift at 505 cm⁻¹ arises from the bending mode of V-O and could have a superposition with the Ni-O vibration, which usually occurs in the same region.^[42,43] The band at 684 cm⁻¹ corresponds to the anti-symmetric stretching mode of V-O-V.^[41] Figure 1h shows the Fourier transform infrared (FTIR) spectrum of Ni_{0.25}V₂O₅·nH₂O with a series of absorption bands which are assigned to different vibration modes of V-O, V-O-V, V=O, Ni-O, O-H and H-O-H respectively, in agreement with previous studies.^[44,45,46,47] In addition to the detection of intermolecular water from the FTIR results, thermogravimetric analysis (TGA) was used to quantify the water content in Ni_{0.25}V₂O₅·nH₂O and determine the weight percentage of crystalline water (Figure 1i). The 6.2 % weight loss in the temperature range of 150-475°C from the TGA curve suggest a stoichiometric formula of Ni_{0.25}V₂O₅·0.74 H₂O for the as-prepared material.

After successfully synthesizing Ni_{0.25}V₂O₅·nH₂O, the material was fabricated into a coin cell with 3M ZnSO₄ electrolyte for the evaluation of electrochemical performance. Figure 2a exhibits galvanostatic charge-discharge profiles of Ni_{0.25}V₂O₅·nH₂O under different current densities from 0.2 to 5 A g⁻¹. Distinct plateaus can be discerned in both charge/discharge processes and a high specific capacity of 402 mAh g⁻¹ at a current density of 0.2 A g⁻¹ was attained. A relatively high specific capacity of 164 mAh g⁻¹ can still be retained after a 25 fold

increase of current density to 5 A g^{-1} . The cycling and rate performance of $\text{Ni}_{0.25}\text{V}_2\text{O}_5 \cdot n\text{H}_2\text{O}$ is further illustrated in Figure 2b, where the current densities was raised stepwise from 0.2 to 5 A g^{-1} and return to 0.2 A g^{-1} with 8 cycles at each current density. Impressively, the $\text{Ni}_{0.25}\text{V}_2\text{O}_5 \cdot n\text{H}_2\text{O}$ material offers very stable charge/discharge performances at different current densities, a high specific capacity and an outstanding capacity retention of 95 % (381 mAh g^{-1}) achieved when the current density was returned to 0.2 A g^{-1} . The recovery of good capacity at higher current density was also observed, *i.e.* $320, 274, 221, 186$ and 147 mAh g^{-1} at $0.5, 1, 2, 3$ and 5 A g^{-1} respectively, with a corresponding Coulombic efficiency (CE) of 99.8 %. In comparison with other reported pre-intercalated V_2O_5 , $\text{Ni}_{0.25}\text{V}_2\text{O}_5 \cdot n\text{H}_2\text{O}$ presents improved capacity and stability. {For comparison $\sigma\text{-Zn}_{0.25}\text{V}_2\text{O}_5 \cdot n\text{H}_2\text{O}$ (300 mAh g^{-1} @ 50 mA g^{-1}),^[17] $\sigma\text{-Mg}_{0.34}\text{V}_2\text{O}_5 \cdot n\text{H}_2\text{O}$ (353 mAh g^{-1} @ 50 mA g^{-1}),^[16] $\text{K}_{0.25}\text{V}_2\text{O}_5$ (85 mAh g^{-1} @ 500 mA g^{-1})^[48] and $\text{Ca}_{0.25}\text{V}_2\text{O}_5 \cdot n\text{H}_2\text{O}$ (340 mAh g^{-1} @ 50 mA g^{-1}),^[21] *etc.* (details in Table S2)}. Figure 2c shows the first three cyclic voltammetry (CV) curves of the $\text{Ni}_{0.25}\text{V}_2\text{O}_5 \cdot n\text{H}_2\text{O}$ electrode at a scan rate of 0.2 mV s^{-1} . It can be noted that multiple redox couples occur, which indicates reversible intercalation/de-intercalation of Zn^{2+} after the first asymmetrical discharge/charge process. The CV curves maintain the same shape and position with certain redox couples, which confirm the stability of $\text{Ni}_{0.25}\text{V}_2\text{O}_5 \cdot n\text{H}_2\text{O}$ in galvanostatic charge-discharge profiles with activation after the initial cycle. Additionally, regular shifting of peaks with increasing scan rates from 0.1 to 0.5 mV s^{-1} were observed, from which a quantitative evaluation of charge storage kinetics in the cathode host can be obtained (Figure S5a). The b values of the notable six redox reaction peaks are $0.39, 0.79, 0.75, 0.60, 0.52$ and 0.64 respectively, indicating mainly diffusion-controlled kinetics (Figure S5b). A further estimation of capacitive and diffusion-controlled behaviour of the cathode materials are illustrated in a CV profile at a scan rate 0.4 mV s^{-1} with 33.5% capacitive contribution among all current response (Figure S5c). An increased fraction of capacitive contribution from 21.5% to 45.3% was observed as the cyclic voltammetry sweep rate was increased from 0.1 mV s^{-1}

to 1 mV s^{-1} . The results indicate that at low sweep rates, kinetics are mainly determined by ionic diffusion, whereas at higher sweep rates, capacitive behaviour becomes an increasingly dominant effect (Figure S5d). Galvanostatic intermittent titration technique (GITT) was employed to study the Zn^{2+} diffusion coefficient within $\text{Ni}_{0.25}\text{V}_2\text{O}_5 \cdot n\text{H}_2\text{O}$ and $\text{Co}_{0.25}\text{V}_2\text{O}_5 \cdot n\text{H}_2\text{O}$ during the insertion/extraction process (Figure S5 e-h). Both of their D values are in range of 10^{-8} to 10^{-10} which indicate improved ion diffusion kinetics compared with previous reported $\text{Zn}_{0.25}\text{V}_2\text{O}_5$ ^[17] and $\text{K}_{0.25}\text{V}_2\text{O}_5$ ^[48]. The long-term durability of $\text{Ni}_{0.25}\text{V}_2\text{O}_5 \cdot n\text{H}_2\text{O}$ under different current densities were studied (Figure 2d, e and S6) with extended cycling tests. Only a 10 % decay of the capacity of the $\text{Ni}_{0.25}\text{V}_2\text{O}_5 \cdot n\text{H}_2\text{O}$ electrode occurred after 50 cycles under a current density of 0.2 A g^{-1} and the specific capacity remained as 347 mAh g^{-1} . In addition to this, a 100 cycle galvanostatic charging/discharging process was carried out, which exhibits only a 15% attenuation (*vs.* the maximum achieved capacity of 406 mAh g^{-1}) after all cycles (Figure S6a). By comparing stability at 1 A g^{-1} with previously reported vanadates, a 23.7% drop after 100 cycles was seen in $\text{NH}_4\text{V}_4\text{O}_{10}$ ^[49], a 31.6 % of capacity attenuation after 50 cycles in $\text{Li}_x\text{V}_2\text{O}_5 \cdot n\text{H}_2\text{O}$ ^[50], 24% reduction of capacity after 500 cycles in $\text{Na}_2\text{V}_6\text{O}_{16} \cdot n\text{H}_2\text{O}$ and 26.5% decrease after 50 cycles in $\text{Cu}_x\text{V}_2\text{O}_5 \cdot n\text{H}_2\text{O}$ ^[23]. Even at a high rate of 5 A g^{-1} , only a 2 % capacity decay (compared with the 2nd cycle with a specific capacity of 218 mAh g^{-1}) after 1200 cycles was obtained. All cycling results exhibit over 99.8 % Coulombic efficiency and highly reversible performance, which was also confirmed by using $3 \text{ M Zn (CF}_3\text{SO}_3)_2$ as an electrolyte for evaluation of long-term stability (Figure S7). The above results imply that $\text{Ni}_{0.25}\text{V}_2\text{O}_5 \cdot n\text{H}_2\text{O}$ is quite robust with various charge/discharge rates and long-term cycling tests in different electrolytes, which present relatively high maximum energy and power density of 286.6 Wh kg^{-1} and 3920.8 W kg^{-1} , respectively, compared with other reported cathodes (Figure S8). The assembled Zn-ion batteries can easily light-up the LED logo lights easily (Inset in Figure 2e). In addition, as-obtained $\text{Co}_{0.25}\text{V}_2\text{O}_5 \cdot n\text{H}_2\text{O}$ was also tested for AZIB cathodes. A specific capacity of 326.8

mAh g⁻¹ with only 0.7 % capacity decline was attained after 30 cycles at the current density of 0.2 A g⁻¹. Meanwhile, a 95 % capacity retention with the discharge capacity of 144.4 mAh g⁻¹ was shown after 500 cycles under 5 A g⁻¹. The rate performance exhibited only 4 % capacity drop when current densities return to 0.5 A g⁻¹ (Figure S9), which represents a lower performance than the Ni_{0.25}V₂O₅·nH₂O electrode, but is still amongst the highest capacities reported for AZIB cathode materials. To investigate the specific capacity variation of Ni_{0.25}V₂O₅·nH₂O and Co_{0.25}V₂O₅·nH₂O, electrochemical impedance spectroscopy (EIS) was carried out to verify different ion transport properties within the electrodes before and after cycling stability measurements (Figure S9). A cycle-dependent ion transport property was observed, since both cycled electrodes of Ni_{0.25}V₂O₅·nH₂O and Co_{0.25}V₂O₅·nH₂O showed much better behaviour than those cathodes prior to cycling. Among cycled electrodes, the Ni_{0.25}V₂O₅·nH₂O electrode presents better performance than Co_{0.25}V₂O₅·nH₂O, demonstrated by a lower inherent resistance ($R_s = 2.85 \Omega$) and more efficient ion diffusion ($R_{ct} = 22.38 \Omega$) for Ni_{0.25}V₂O₅·nH₂O compared to Co_{0.25}V₂O₅·nH₂O ($R_s = 4.82 \Omega$, $R_{ct} = 59.77 \Omega$), measured under identical conditions, which could be interpreted by potential Coulomb repulsion forces between cations even though a larger d-space attained in Co_{0.25}V₂O₅·nH₂O lattice.^[51] Thus, the higher performance of Ni_{0.25}V₂O₅·nH₂O can be attributed to superior ion-diffusion properties, which highlights the importance of the type of pre-intercalated cation within the ‘double-layer’ V₂O₅ framework prior to the measurement (Figure S10, Table S3). Additionally, a slight modification of the synthetic process (without adding nickel and cobalt acetate) was performed to produce vanadium oxides without neither Ni nor Co to evaluate the importance of pre-intercalated ions in vanadate framework. The XRD pattern of as-obtained vanadium oxide in Fig. S11 (a) matches well with V₃O₇·H₂O (JCPDS 28-1433). It is seen that the added nickel (cobalt) precursor can substantially affect the enthalpy of formation in the reaction process forming different products. A mixed valence states within 4 to 5 in V₂O₅ frameworks strongly involve with pre-intercalated ions, and probably hardly formed in this

reaction circumstance. Notably, the investigation of crystallography of $V_3O_7 \cdot H_2O$ presents a lattice structure of V_3O_8 layered slabs only consisting of VO_5 and VO_6 polymorphs^[52], which possess similar feature of specific crystallography characteristics as described in δ - $Ni_{0.25}V_2O_5 \cdot nH_2O$. Additionally, electrochemical measurements were carried out for comparison with δ - $Ni_{0.25}V_2O_5 \cdot nH_2O$. Figure S11 (c) illustrates first 3 cycles of CV plots of $V_3O_7 \cdot H_2O$ with mainly two stable pairs of redox peaks, and the following galvanostatic charge/discharge exhibit a large initial capacity of 354 mAh g^{-1} and 225 mAh g^{-1} at current densities of 0.2 and 5 A g^{-1} , respectively. However, a poor cycling stability and rate performance can be observed in Figure S11(d-f), that is, a 58.4% and 50% drop of capacities for 50 and 5000 cycles at 0.2 A g^{-1} and 5 A g^{-1} , respectively. The unsatisfactory performance could be regarded as fast deterioration of structure due to the strong electrostatic force, thus, introducing pre-intercalated ions could be one of promising solution.^[18,19,20] Moreover, it is inevitable to consider proton existing in adopted mild acidic electrolyte, which could possibly participate in intercalation in the cathode. In order to elucidate potential proton intercalation contributing to the electrochemical capacity, we conducted additional galvanostatic charge-discharge measurement through a three-electrode configuration in dilute H_2SO_4 ($pH \approx 4$) electrolyte (Fig. S12). The results illustrate an initial specific capacity of 51 mAh g^{-1} and 34 mAh g^{-1} in discharged and charged states, respectively. Subsequently, the capacity rapidly decay to $\sim 30 \text{ mAh g}^{-1}$ in the rest of cycles. Similar phenomenon can be also observed in previous reports on vanadium-based cathodes.^[53,54,55] Therefore, the nearly irreversible insertion/extraction reaction and negligible contribution to capacity from proton intercalation indicate that the Zn^{2+} intercalation mechanism mainly dominate in as-prepared cathode material and it will be further confirmed by the following multiple *ex-situ* characterizations. Combined *ex-situ* X-ray photoelectron spectroscopy (XPS), XRD and TEM analyses were carried out to investigate the possible Zn^{2+} insertion/extraction in the $Ni_{0.25}V_2O_5 \cdot nH_2O$ electrode. To verify the different chemical states upon pristine and charged/discharged

$\text{Ni}_{0.25}\text{V}_2\text{O}_5 \cdot n\text{H}_2\text{O}$ electrodes, *ex-situ* XPS experiments were performed on the pristine, fully discharged and fully charged electrodes. The results shown in Figure 3a clearly illustrate the variation of binding energies and valence states in the V 2p region, which can be assigned to the insertion/extraction of Zn^{2+} . More explicitly, the multivalent states of V^{5+} and V^{4+} that occur in pristine $\text{Ni}_{0.25}\text{V}_2\text{O}_5 \cdot n\text{H}_2\text{O}$ are consistent with other reported pre-intercalated V_2O_5 frameworks showing partial reduction. Although the evolution of V^{5+} ($2p_{3/2}$: 517.5 eV) and V^{4+} sites ($2p_{3/2}$: 516.2 eV) in both pristine and fully discharged states of $\text{Ni}_{0.25}\text{V}_2\text{O}_5 \cdot n\text{H}_2\text{O}$ maintain almost the same binding energy, a noteworthy reduction of the V oxidation state was observed through an obviously intensified V^{4+} component, and the distinct peak appearing at 515.5 eV which can be assigned to V^{3+} species. Analysis of peak area proportion indicates a notable drop of the average valence state of V species, reduced from $\text{V}^{4.69+}$ to $\text{V}^{4.03+}$ in pristine and fully discharged $\text{Ni}_{0.25}\text{V}_2\text{O}_5 \cdot n\text{H}_2\text{O}$ respectively. In fully charged $\text{Ni}_{0.25}\text{V}_2\text{O}_5 \cdot n\text{H}_2\text{O}$, the V^{3+} component vanishes, while a dominant peak at a binding energy of 517.6 eV and a relatively weaker peak at 516.3 eV appear, which are similar to the pristine and discharged electrodes. These peaks can be assigned to V^{5+} and V^{4+} respectively, resulting in an average valence of $\text{V}^{4.78+}$. The above results demonstrate that highly reversible redox reactions of V species occur during the insertion/extraction of Zn^{2+} . Additionally, Ni species in $\text{Ni}_{0.25}\text{V}_2\text{O}_5 \cdot n\text{H}_2\text{O}$ were also determined by XPS (Figure 3b). The dominant peak at a binding energy of 865.3 eV corresponds to Ni^{2+} $2p_{3/2}$. It is hard to retrieve the exact peak position of Ni 2p in the cycled electrodes, since the signal displays a weak intensity. This is likely due to a partial deintercalation of Ni upon insertion and removal of Zn^{2+} , combined with interference from binder and carbon mixed electrode, a further characterization of the varied Ni amount in electrode will be discussed below from an *ex-situ* Energy Dispersive Spectroscopy (EDS) measurement. The phenomenon is also reported in other AZIB electrodes, and is probably due to a displacement/intercalation reaction mechanism.^[7,56,57,58,60] Figure 3c presents the XPS region of Zn 2p for the fully discharged and charged electrodes. An intense Zn^{2+} $2p_{3/2}$ peak

at 1023.4 eV corresponds to the intercalated Zn^{2+} in $\text{Ni}_{0.25}\text{V}_2\text{O}_5 \cdot n\text{H}_2\text{O}$ at the fully discharged state, while a lower intensity signal at 1022.1 eV in the fully charged electrode indicates some residual Zn^{2+} remains in the structure upon cycling, consistent with previous studies.^[16,17]

After clarifying the variation of chemical states, *ex-situ* XRD and TEM studies were performed to uncover the structural evolution of materials during charge/discharge processes. As displayed in Figure 3d, the dynamic structural evolution of $\text{Ni}_{0.25}\text{V}_2\text{O}_5 \cdot n\text{H}_2\text{O}$ upon different charge/discharge states between the 1st and 20th cycles were elucidated at a current density of 0.2 A g⁻¹ via *ex-situ* XRD analysis. At first, the electrode was immersed into an electrolyte for 48 h and was measured to compare with pristine $\text{Ni}_{0.25}\text{V}_2\text{O}_5 \cdot n\text{H}_2\text{O}$ materials. Notably, a negligible change of the crystal planes after immersion was observed, which implies the $\text{Ni}_{0.25}\text{V}_2\text{O}_5 \cdot n\text{H}_2\text{O}$ crystal structure is stable in the electrolyte. Upon a deep discharge in the first cycle to 0.3 V, the 2θ of (001) reflection shifts from 3.94° to 3.76°, and the d-space for (001) plane slightly expands from 10.3 Å to 10.8 Å after $\text{Zn}^{2+}/\text{H}_2\text{O}$ insertion. Unlike a significant contraction of the interlayer d-space in the first fully discharged state of previously reported $\sigma\text{-Zn}_{0.25}\text{V}_2\text{O}_5 \cdot n\text{H}_2\text{O}$,^[17] the observations in the present study match well with a recent work investigating V_3O_8 as a layered host for AZIBs.^[60] In addition, it is worth noting that once Zn^{2+} is introduced into the host $\text{Ni}_{0.25}\text{V}_2\text{O}_5 \cdot n\text{H}_2\text{O}$ lattice, the $\text{Zn}_x\text{Ni}_y\text{V}_2\text{O}_5 \cdot n\text{H}_2\text{O}$ phase becomes highly reversible after many cycles, recovering the same reflection site in each fully discharged state. Analogously, a reversible change of the d-space along *c*-axis from 10.8 Å to 13.5 Å was observed when the electrodes were charged to 1.7 V in both the 1st and 20th cycles. The expansion to 13.5 Å has been interpreted as the incorporation of more H_2O molecules from the electrolytes after the extraction of Zn^{2+} .^[61] It can also be noted that a reversible shift of the peak positions occurs at exactly the same reflection range on the (001) plane during the charge/discharge processes, that is, the peak shifts occur consistently in the same 2θ range upon each cycle, returning each time to the same position. More specifically, the d-space of the fully charged $\text{Ni}_{0.25}\text{V}_2\text{O}_5 \cdot n\text{H}_2\text{O} // \text{Zn}$

(13.5 Å) initially drops to 10.5 Å upon discharging to 1.2 V, followed by a slight increase of d-space to 11.2 Å when further discharged to 0.75 V. Similarly, each of the two charged states at 0.8 V and 1.25 V exhibit the same (001) d-space of 11.2 Å and 10.5 Å respectively. Due to the formation of a Zn^{2+} complex with H_2O during intercalation/de-intercalation within the host $\text{Ni}_{0.25}\text{V}_2\text{O}_5$ electrode, it is difficult to elucidate the phase changes occurring concurrently to the evolution of interlayer spacings. However, it can be assumed that the large contraction of interlayer spacing from 13.5 Å during the initial stages of discharge can be attributed to the displacement of free and structural water molecules by the first intercalated Zn^{2+} ions. A slight fluctuation of the (001) d-space around the fully discharged states (10.8 Å) can be associated with a rearrangement of guest ions within the host structure. A regular reversible shift of (600) (*a*-axis), (020) (*b*-axis) and (711) planes in a small region upon the discharge and charge processes respectively, display opposite motion compared with {001} planes, indicating an expansion/contraction of the lattice towards both *a* and *b* axis, resulting in a three dimensional evolution of a single phase crystal structure. This behaviour contrasts with most other reported hydrated vanadium bronze AZIB cathode materials, which tend to generate coexisting multiphases indicated by split reflections around (001) and other correlated crystal planes. All reflection peaks observed in the *ex-situ* XRD plots in this work are derived from pristine $\text{Ni}_{0.25}\text{V}_2\text{O}_5 \cdot n\text{H}_2\text{O}$, which demonstrates that the host $\text{Ni}_{0.25}\text{V}_2\text{O}_5 \cdot n\text{H}_2\text{O}$ electrode exhibits highly reversible, robust and flexible capability for AZIB applications. A further investigation of structural evolution was verified by *ex-situ* TEM with distinct variation of d-space of the (004) plane in fully discharged/charged states of the $\text{Ni}_{0.25}\text{V}_2\text{O}_5 \cdot n\text{H}_2\text{O}$ electrode (Figure S13). In confirmation of the *ex-situ* XRD results, a relatively narrow d-space of 0.27 nm corresponding to (004) plane in the fully discharged state is in accordance with a contraction of the lattice along the *c*-axis, whereas an expanded plane of 0.34 nm related to the (004) plane was observed in the fully charged state. Additionally, *ex-situ* SEM and EDS characterizations of the zinc anode were adopted to

observe the morphology and elemental variation after 100 cycles. It was seen that small amount of dendritic formation occurred on the surface of the zinc anode, and only a small amount of sulfur element was present, which is reasonably explained as being derived from the zinc sulphate electrolyte (Figure S14). *Ex-situ* EDS was performed on the as-prepared electrodes after 1 and 20 charge/discharge processes, and the results are shown in Figure S15. From the results, chemical formulae of $\text{Ni}_{0.23}\text{V}_2\text{O}_5 \cdot n\text{H}_2\text{O}$, $\text{Ni}_{0.23}\text{ZnV}_2\text{O}_5 \cdot n\text{H}_2\text{O}$, $\text{Ni}_{0.11}\text{Zn}_{0.9}\text{V}_2\text{O}_5 \cdot n\text{H}_2\text{O}$, $\text{Ni}_{0.19}\text{Zn}_{1.16}\text{V}_2\text{O}_5 \cdot n\text{H}_2\text{O}$ and $\text{Ni}_{0.11}\text{Zn}_{0.27}\text{V}_2\text{O}_5 \cdot n\text{H}_2\text{O}$ can be detected, corresponding to the pristine, initial discharge, initial charge, 20th cycle discharge and 20th cycle charge states of cathode materials respectively. This indicates a highly reversible insertion/extraction mechanism for the Ni component, concurrently with the insertion and removal of the zinc ions. In contrast, the pristine $\text{Co}_{0.23}\text{V}_2\text{O}_5 \cdot n\text{H}_2\text{O}$ electrode experienced distinct loss of Co content after cycling, and chemical formulae of $\text{Co}_{0.23}\text{Zn}_{1.3}\text{V}_2\text{O}_5 \cdot n\text{H}_2\text{O}$, $\text{Co}_{0.08}\text{Zn}_{0.29}\text{V}_2\text{O}_5 \cdot n\text{H}_2\text{O}$, $\text{Co}_{0.06}\text{Zn}_{1.09}\text{V}_2\text{O}_5 \cdot n\text{H}_2\text{O}$ and $\text{Co}_{0.05}\text{Zn}_{0.34}\text{V}_2\text{O}_5 \cdot n\text{H}_2\text{O}$ can be obtained for the 1st discharge, 1st charge, 20th discharge and 20th charge states, respectively. Evidently, the removal of Co ions is irreversible during charge/discharge processes, giving rise to inferior cycling capability compared with $\text{Ni}_{0.25}\text{V}_2\text{O}_5 \cdot n\text{H}_2\text{O}$. The inferior cycling is observed in galvanostatic long-term measurements in Figure S9. Additionally, *ex-situ* Raman spectra of varied charging/discharging states of the electrodes were obtained (Fig.S16). The Raman shifts of all tested $\text{Ni}_{0.25}\text{V}_2\text{O}_5 \cdot n\text{H}_2\text{O}$ materials remain at almost the same positions during the various states. The only notably change is the appearance of a small split peak emerging, occurring at 153 cm^{-1} in the fully charging electrode after 20 galvanostatic treatment cycles. This can be interpreted due to small amount loss of the pre-intercalated Ni ions in the lattice^[62], resulting in slight weakening of the interaction between the V_2O_5 double-layers. Notably, the equivalent peak in $\text{Co}_{0.25}\text{V}_2\text{O}_5 \cdot n\text{H}_2\text{O}$ appears at a lower Raman shift of 142 cm^{-1} and is accompanied simultaneously by a redshifting of the peak at 1006 cm^{-1} when the material is charged. The results of our *ex-situ* EDS and *ex-situ* Raman measurements are

consistent with the previous observations and indicate that the $\text{Ni}_{0.25}\text{V}_2\text{O}_5 \cdot n\text{H}_2\text{O}$ cathode is a robust structure, with a highly reversible Zn intercalation mechanism.

Additionally, *ex-situ* near edge X-ray absorption fine structure (NEXAFS) were carried out to interpret the electronic and coordination configuration of the as-obtained cathode materials. In Figure 4a, Ni L-edge NEXAFS spectra provide information of electron dipole-allowed transition from Ni $2p$ to the $3d$ unoccupied valence states. There are two major absorption features result from the spin-orbital splitting: L_3 -edge ($2p_{3/2}$ to $3d$, 850-855 eV) and L_2 -edge ($2p_{1/2}$ to $3d$, 862-872 eV) ^[63,64]. The multiplets at L_3 -edge reveals the high spin Ni^{2+} electronic structure and nearly octahedral coordination structure (O_h) for all samples ^[65]. In the O_h point group of d^8 electronic configuration, the ground state symmetry is ${}^3A_{2g}$ (e_g^2) and the configurational state of $2p$ - $3d$ transition is $2p_{3/2} d^9$ (the underscore refers to the core hole at $2p_{3/2}$) ^[66-69]. Due to the ligand metal p - d charge transfer (LMCT), additional ground state $d^9 \underline{L}$ will mix with $d^8 L$ state and contribute to the spectra. Thus two absorption peaks could be found at the L_3 -edge, attributed to $d^8 L$ ground state (Peak A, 851.4 eV) and $d^9 \underline{L}$ ground state (Peak B, 853.4 eV), respectively. ^[66-69] The energy difference between the two peaks mainly depends on the p - d charge transfer energy Δ and d - p hybridisation strength. ^[66-69] In this figure, a shift of the peak B towards higher energy for discharged cathode material could be found, indicating an increase in p - d charge transfer energy Δ and less d - p hybridisation within the discharged sample. Given the fact that two O anions of $[\text{NiO}_6]$ are shared with VO_x layers, the other four O anions will be shared with $[\text{ZnO}_6]$ after discharging process. Thus the insertion of Zn^{2+} into VO_x layers is expected to perform additional d - p hybridisation (Zn $3d$ and O $2p$) and withdraw the O $2p$ electrons towards Zn^{2+} , leading to the rise of p - d charge transfer energy Δ (O $2p$ to Ni $3d$) and less d - p hybridisation strength (O $2p$ and Ni $3d$). Furthermore, the Ni^{2+} could be stabilized in the cathode during the charging and discharging process, compared to $\text{Co}_{0.25}\text{V}_2\text{O}_5$ in which the Co^{2+} completely leached out after charging and discharging cycles observed in previous discussion of *ex-situ* Raman and *ex-situ* EDS.

Additionally, Figure 4b shows the V L-edge and O K-edge NEXAFS spectra. the V L-edge includes two main peaks, which are L₃-edge (515-520 eV) and L₂-edge (520-528 eV), corresponding to the V 2p_{3/2} to V 3d and V 2p_{1/2} to V 3d dipole allowed transition, respectively.^[70-74] The O K-edge is located after 527 eV, indicating electron transition from O 1s to valence *p-d* hybridising orbitals.^[70-74] The shape and position of V L₃-edge spectra of fresh and charged samples could be attributed to a mixture of V⁵⁺ and V⁴⁺ oxidation state. The V⁵⁺ and V⁴⁺ in [VO₆] octahedra structure present C_{4v} and D_{4h} symmetry, respectively, result in additional split of *t_{2g}* and *e_g* orbitals into *e* (*d_{yz}*, *d_{xz}*), *b₂* (*d_{xy}*), *a₁* (*d_z²*) and *b₁* (*d_x²-y²*) orbitals in order of energy level.^[67-71] In this figure, the peaks accrued at 515.2 and 516.4 eV are considered to be 2p_{3/2} to *e* and *b₂* transitions, and the highest peak at 518.0 eV is contributed from 2p_{3/2} to *a₁* and *b₁* transitions. For O K-edge, the first peak at 529.0 eV arises from final states of *e* and *b₂*, while the second peak at 531.6 reveals the transition to *a₁* and *b₁* states. As showed in the figure, a major difference could be found between the charged and discharged sample: the V 2p_{3/2} to *e* and *b₂* transition and O 1s to *e* and *b₂* transition present much weaker absorption features in discharged samples. This is an evidence of higher electron filled density (lower density of vacancies) in *e/b₂* orbitals, indicating a reduction of V to more V³⁺/V⁴⁺ content within the discharged cathode material. It is also worth mentioning that the tiny peak at 511.2 eV is a second order absorption feature of Zn L₃-edge (originally should be at 1022 eV), proving the present of Zn species. For comparison, Co L₃-edge and L₂-edge X-ray absorption spectroscopy could directly probe the electron dipole-allowed transition from Co 2p to the 3d unoccupied valence states, which will provide information of electronic configuration and oxidation state of Co. The spin-orbit interaction splitting the 2p core states into 2p_{1/2} and 2p_{3/2} core levels, which corresponds to the well separated L₂ (790-795 eV) and L₃ (775-785 eV) absorption features, respectively^[75]. In Figure 4c, the general line shape of fresh cathode material is in good agreement with high spin Co²⁺ in CoO, suggesting the Co²⁺ ions are octahedral coordinated with O atoms.^[65-77] The shoulder peak at 775.8 eV is also

characteristic for Co^{2+} octahedral coordination.^[75] For the charged and discharged cathode materials, no Co absorption could be probed, indicating leaching of Co after cycling process and will not re-insert into the cathode (instability of Co-V-O). Moreover, a similar results of V L-edge and O K-edge NEXAFS spectra of $\text{Co}_{0.25}\text{V}_2\text{O}_5\cdot n\text{H}_2\text{O}$ are observed in Figure 4d, which present an analogous shape and position shift of the V L_3 -edge spectra in fresh and charged/discharged sample, which are attributed to varied vanadium ion oxidation states.

To understand the intercalation mechanism of Zn^{2+} in $\text{Ni}_{0.25}\text{V}_2\text{O}_5\cdot n\text{H}_2\text{O}$ at the atomic-level, we performed density functional theory (DFT) calculations using the dispersion-corrected hybrid-exchange B3LYP-D3 functional, implemented in the CRYSTAL17 code.^[78] Full details of the calculations can be found in the Supplementary Information.

For computational ease, we used a model of composition $\text{Ni}_{0.25}\text{V}_2\text{O}_5\cdot \text{H}_2\text{O}$. The structure is well reproduced by the calculations, with lattice parameters within ± 1 % of experimental values (Table S4).

When viewed along the b crystallographic axis, two channels can be defined in the structure (Figure 5a). Half of the sites in channel I are occupied by Ni^{2+} ions. Channel II is unoccupied, providing pathways for Zn^{2+} diffusion along the b direction. Under dilute Zn^{2+} intercalation conditions, during the initial stages of the first discharge, there are 4 possible Zn^{2+} insertion sites, denoted A – D, and illustrated in Figure 5b. Site A is in channel I; sites B, C and D are in channel II. The optimised geometry of Zn^{2+} ions in each site, along with their relative energies are shown in Figure 5c. Sites A and D are the most stable locations and are nearly isoenergetic ($\Delta E = 0.039$ eV). In these sites, Zn^{2+} ions are approximately octahedral, located between two NiO_6 octahedra with which they share edges. Zn ions further coordinate to two axial O-ion in the V_2O_5 layers. In site A, Zn^{2+} ions have slightly distorted O-Zn-O axial bonds, which is due to a cooperative contraction of the interlayer space caused by the Zn ions. This contrasts to the linear O-Ni-O axial bonds for adjacent Ni^{2+} ions in channel I (Figure S18). In site D, neighbouring NiO_6 octahedra rotate, stabilising the Zn^{2+} ion between them,

with axial O-Zn-O bonds tilted in the opposite direction to the adjacent Ni-O axial bonds (Figure S18).

In B and C sites (channel II), the Zn^{2+} ions coordinate to two O ions in one V_2O_5 layer and one O ion in the adjacent layer, and form either three (site B) or two (site C) bonds to H_2O molecules in the ab plane. B sites are +0.356 eV, and C sites +0.695 eV higher in energy relative to A sites, with the energy difference between the B and C attributed to the higher and more favourable coordination that Zn^{2+} ions achieve in the B sites. In both B and C sites, the Zn^{2+} ions are displaced along the c axis towards the V_2O_5 layer in which they coordinate to two O ions. For Zn^{2+} insertion in each of these sites, which corresponds to a stoichiometry of $\text{Zn}_{0.125}\text{Ni}_{0.25}\text{V}_2\text{O}_5\cdot\text{H}_2\text{O}$ there is a contraction of the interlayer separation (the c -axis) compared to the pristine material (Table S4), as the Zn^{2+} ions ‘pin’ the V_2O_5 sheets closer together. This is consistent with the computational results of Wu *et al.*,^[79] who investigate Zn intercalation in $\text{V}_2\text{O}_5\cdot\text{H}_2\text{O}$. We initially investigated Zn^{2+} mobility along channel II at dilute Zn concentration. To traverse a unit cell, thus allowing mobility through the structure, the Zn^{2+} ions must follow the pathways between sites in the order of $\text{B} \rightarrow \text{D} \rightarrow \text{B} \rightarrow \text{C} \rightarrow \text{C} \rightarrow \text{B}$ (Figure S19), which then repeats in the next unit cell.

Figure 5d-f show the energy profile of this migration pathway. The maximum activation barrier for an individual jump is < 0.5 eV, indicating that Zn^{2+} diffusion can occur relatively rapidly along channel II at room temperature. The migration pathway along channel II follows a ‘zig-zag’ pattern when the structure is viewed along the a axis, due to the preference of the Zn^{2+} ions to coordinate closer to one of the V_2O_5 layers than the other in each type of site (Figure S20). To occupy channel I, Zn^{2+} ions must move from site C to site A. The energy profile for this migration is shown in Figure 5g, and the activation barrier is +0.563 eV. However, since A sites are more stable by ~ 0.69 eV than C sites, the barrier for the reverse migration from A to C is +1.2 eV. This activation energy will not be overcome frequently at room temperature, and thus Zn^{2+} ions will tend to accumulate in A sites (Figure S21). Thus,

on initial cell discharge, Zn^{2+} ions will be able to migrate along the whole length of channel II, and overcome the barrier to move from site C in channel II, to site A in channel I. When sites A along channel I are all filled, resulting in a stoichiometry of $\text{Zn}_{0.25}\text{Ni}_{0.25}\text{V}_2\text{O}_5\cdot\text{H}_2\text{O}$ (Figure 4h), Zn^{2+} ions will still be able to migrate along the open channel II, indicating a mechanism for further intercalation. Since the backward barrier for extraction of Zn^{2+} ions from site A will not be achieved at room temperature, yet experimentally the extraction of Zn^{2+} is observed upon charge, a structural rearrangement must occur upon intercalation of Zn^{2+} beyond $\text{Zn}_{0.25}\text{Ni}_{0.25}\text{V}_2\text{O}_5\cdot\text{H}_2\text{O}$. The rearrangement will then allow Zn^{2+} ions (and Ni^{2+}) to be removed from the structure upon charge, from the fully discharged electrode.

To understand the structure of $\text{Zn}_x\text{Ni}_{0.25}\text{V}_2\text{O}_5\cdot\text{H}_2\text{O}$ when $x > 0.25$, we extended our investigations by adding additional Zn^{2+} ions to the model of $\text{Zn}_{0.25}\text{Ni}_{0.25}\text{V}_2\text{O}_5\cdot\text{H}_2\text{O}$ with all A sites filled. Addition of more Zn into channel II, to a stoichiometry of $\text{Zn}_{0.375}\text{Ni}_{0.25}\text{V}_2\text{O}_5\cdot\text{H}_2\text{O}$ causes a progressive contraction of the interlayer c parameter, and a decreased axial O-Zn-O bond angle for the octahedral Zn ions in A sites. Eventually, the V_2O_5 sheets become too close together for Zn ions in site A in channel I to retain their octahedral coordination, and a structural re-arrangement occurs. The A site Zn ions are displaced along the a lattice direction, bonding to two O-ions in one V_2O_5 layer, and one in the adjacent layer (Figure S22).

At a stoichiometry of $\text{Zn}_{0.5}\text{Ni}_{0.25}\text{V}_2\text{O}_5\cdot\text{H}_2\text{O}$, the stable Zn ordering is for two Zn ions to both occupy a position between the A site previously occupied by only one Zn^{2+} , resulting in a ‘split interstitial’ geometry (Figure 5h). This type of geometry can be described as ‘frustrated’, since the Zn ions are no longer in an optimal coordination environment. Such frustration raises the energy of the Zn ions and lowers the activation barriers for migration compared to the most stable intercalation sites.^[80] It is possible that the ‘split interstitial’ Zn^{2+} ions are mobile in the structure and can be removed upon charge *via* a correlated interstitialcy mechanism.

At a stoichiometry of $\text{Zn}_{0.5}\text{Ni}_{0.25}\text{V}_2\text{O}_5\cdot\text{H}_2\text{O}$, the calculations indicate that some dissociation of the interlayer H_2O molecules occurs within V_2O_5 interlayer space (Figure 5f), which has been described previously both from DFT results^[79] and FTIR spectroscopy of solvated protons in $\text{V}_2\text{O}_5\cdot n\text{H}_2\text{O}$ gels.^[81] Dissociated water introduces significant complexity to the system, and we therefore did not attempt to evaluate the structure of the fully discharged electrode in our calculations. The experimental XRD presented in Figure 3d reveals that the interlayer space is expanded for the fully discharged electrode (10.8 Å), compared to the pristine material (10.3 Å). From our DFT studies, we observe a progressive contraction of the c parameter as Zn is added (Table S4), however it should be noted that we consider intercalation only up to $x = 0.5$ in $\text{Zn}_x\text{Ni}_{0.25}\text{V}_2\text{O}_5\cdot\text{H}_2\text{O}$. Beyond this point, we expect that as x in $\text{Zn}_x\text{Ni}_{0.25}\text{V}_2\text{O}_5\cdot\text{H}_2\text{O}$ is increased beyond 0.5, the interlayer separation begins to expand again. The DFT results reported by Wu *et al.* show a contraction of the unit cell volume between $0 < x < 0.5$, in $\text{Zn}_x\text{V}_2\text{O}_5\cdot\text{H}_2\text{O}$, followed by an expansion when $x > 0.5$, which support both our DFT and experimental XRD results.

The calculated intercalation voltages per Zn ion for $x = 0.25$ and 0.5 in $\text{Zn}_x\text{V}_2\text{O}_5\cdot\text{H}_2\text{O}$ are 1.426 and 1.087 V respectively (Table S4), with a separation of 0.339 V. These values, and their difference, closely correspond to the first two peaks in the discharge CV curve in Figure 2c, beyond the first cycle. This indicates that Zn^{2+} intercalation proceeds *via* a staging mechanism, where all A sites are filled first between $0 < x < 0.25$, followed by filling of the ‘split-interstitial’ sites between $0.25 < x < 0.5$. The small variation between calculated and experimental voltage can be attributed to structural changes occurring upon the first discharge/charge cycle.

A full analysis of the electronic density of states, spin density isosurfaces and Mulliken charges on the atoms are included in the ESI, Figures S23 – S27 and Table S4-S6.

In addition to the atomic-level simulation of Zn^{2+} insertion/extraction within the $\text{Ni}_{0.25}\text{V}_2\text{O}_5\cdot n\text{H}_2\text{O}$ electrodes using DFT, the macroscopic 3D morphology of the fabricated

electrode, *i.e.* $\text{Ni}_{0.25}\text{V}_2\text{O}_5 \cdot n\text{H}_2\text{O}$ materials coated on hydrophilic carbon paper, was examined using X-ray micro-Computed Tomography (CT) (Figure 6a), which depicts a thin and rough layer of $\text{Ni}_{0.25}\text{V}_2\text{O}_5 \cdot n\text{H}_2\text{O}$ sitting above the carbon fibre base. A close-up image from the reconstructed virtual slice (Figure 6b) displays fairly fine microstructures both in the solid electrode and tiny pores, which are beyond the imaging resolution of the X-ray micro-CT. Thus, higher resolution (nano-CT) was pursued in order to capture the full details of the electrode, with the results presented in Figure 6c. The pore (black), $\text{Ni}_{0.25}\text{V}_2\text{O}_5 \cdot n\text{H}_2\text{O}$ (light grey) and carbon (dark grey) phases are easy to distinguish due to the improved resolution contrast. After extracting the pore phases according to the grey scale level using thresholding segmentation, the skeleton of the pore phase colour-coded by the pore size distribution can be visualised (Figure 6d), from which a complex 3D structure and broad distribution of the pore size are observed. Figure 6e exhibits the streamlines of the diffusion flux simulated based on the reconstructed pore structure. The porosity ε is measured to be 0.18 and the tortuosity factor is computed to be 2.57, giving an effective diffusion coefficient of 0.07, which represents a much better reactant transport capability than those in the LIBs.^[82]

3. Conclusion

Self-templated porous hydrated $\delta\text{-Ni}_{0.25}\text{V}_2\text{O}_5$ nanoribbons were synthesized by a simple one-step hydrothermal method. The materials were found to possess a high reversible capacity of 402 mAh g⁻¹ at 0.2 A g⁻¹ and excellent electrochemical stability with notable 98 % capacity retention after 1200 cycles at a high current density of 5 A g⁻¹. Multi-scale experimental analytical techniques and DFT calculations were employed to elucidate the energy storage mechanism. DFT calculations revealed the dependence of Zn^{2+} intercalation and diffusion properties on the atomic-level arrangement of the cathode, highlighting the important roles of both pre-intercalated ions and host ‘double-layer’ V_2O_5 structure, and suggest routes for the

rational design of hydrated vanadium bronze materials with clearly defined microstructures. A concerted effort was made to boost diffusion kinetics by combining the highly mesoporous nanoribbons with a hydrophilic carbon paper support, with the intention of increasing the interfacial reaction. This resulted in high reactant transport in the electrode, confirmed using the X-ray nano-CT technique.

4. Experimental Section

Experimental details are in Supporting Information.

5. Supporting Information

Supporting Information is available from the Wiley Online Library or from the author.

Acknowledgements

J.L. thanks the funding support from China Scholarship Council/University College London for the joint PhD scholarship. The authors would like to thank Engineering and Physical Sciences Research Council (EPSRC, EP/L015862/1, EP/R023581/1) for funding support and session ID (MG-21641, SI-24197) and the institute (E01 beamline of electron Physical Science Imaging Centre (ePSIC) at Diamond Light Source (DLS) and Diamond Light Source (DLS) B07-1 beamline). KM and FC acknowledge membership of the UK's HEC Materials Chemistry Consortium, which is funded by EPSRC (EP/L000202, EP/R029431), for access to the ARCHER UK National Supercomputing Service (<http://www.archer.ac.uk>), and the UK Materials and Molecular Modelling Hub (MMM Hub), which is partially funded by EPSRC (EP/P020194), for computational resources. KM and FC also acknowledge the use of the UCL Grace High Performance Computing Facility (Grace@UCL), and associated support services, in the completion of this work

Received: ((will be filled in by the editorial staff))

Revised: ((will be filled in by the editorial staff))

Published online: ((will be filled in by the editorial staff))

References

- [1] V. Etacheri, R. Marom, R. Elazari, G. Salitra, D. Aurbach, *Energy Environ. Sci.* **2011**, *4*, 3243–3262.
- [2] H. Kim, J. Hong, K.-Y. Park, H. Kim, S.-W. Kim, K. Kang, *Chem. Rev.* **2014**, *114*, 11788–11827.

- [3] J. Lai, H. Zhu, X. Zhu, H. Koritala, Y. Wang, *ACS Appl. Energy Mater.* **2019**, *2*, 1988–1996.
- [4] C. Xu, B. Li, H. Du, F. Kang, *Angew. Chem. Int. Ed.* **2012**, *51*, 933–935.
- [5] J. Zhou, L. Shan, Z. Wu, X. Guo, G. Fang, S. Liang, *Chem. Commun.* **2018**, *54*, 4457–4460.
- [6] F. Wang, O. Borodin, T. Gao, X. Fan, W. Sun, F. Han, A. Faraone, J. A. Dura, K. Xu, C. Wang, *Nat. Mater.* **2018**, *17*, 543–549.
- [7] G. Li, Z. Yang, Y. Jiang, C. Jin, W. Huang, X. Ding, Y. Huang, *Nano Energy* **2016**, *25*, 211–217.
- [8] Z. Jia, B. Wang, Y. Wang, *Mater. Chem. Phys.* **2015**, *149*, 601–606.
- [9] N. Zhang, F. Cheng, Y. Liu, Q. Zhao, K. Lei, C. Chen, X. Liu, J. Chen, *J. Am. Chem. Soc.* **2016**, *138*, 12894–12901.
- [10] B. Lee, H. R. Lee, H. Kim, K. Y. Chung, B. W. Cho, S. H. Oh, *Chem. Commun.* **2015**, *51*, 9265–9268.
- [11] L. Li, Q. Zhao, Z. Luo, Y. Lu, H. Ma, J. Hu, Y. Li, J. Chen, L. Liu, W. Huang, *Sci. Adv.* **2018**, *4*, eaao1761.
- [12] G. Dawut, Y. Lu, L. Miao, J. Chen, *Inorg. Chem. Front.* **2018**, *5*, 1391–1396.
- [13] M. Winter, R. J. Brodd, *Chem. Rev.* **2004**, *104*, 4245–4270.
- [14] G. S. Gautam, P. Canepa, R. Malik, M. Liu, K. Persson, G. Ceder, *Chem. Commun.* **2015**, *51*, 13619–13622.
- [15] F. Wan, L. Zhang, X. Dai, X. Wang, Z. Niu, J. Chen, *Nat. Commun.* **2018**, *9*, 1656.
- [16] F. Ming, H. Liang, Y. Lei, S. Kandambeth, M. Eddaoudi, H. N. Alshareef, *ACS Energy Lett.* **2018**, *3*, 2602–2609.
- [17] D. Kundu, B. D. Adams, V. Duffort, S. H. Vajargah, L. F. Nazar, *Nat. Energy* **2016**, *1*, 16119.
- [18] X. Yao, Y. Zhao, F. A. Castro, L. Mai, *ACS Energy Lett.* **2019**, *4*, 771–778.
- [19] P. He, G. Zhang, X. Liao, M. Yan, X. Xu, Q. An, J. Liu, L. Mai, *Adv. Energy Mater.* **2018**, *8*, 1702463.
- [20] M. Yan, P. He, Y. Chen, S. Wang, Q. Wei, K. Zhao, X. Xu, Q. An, Y. Shuang, Y. Shao, K. T. Mueller, L. Mai, J. Liu, J. Yang, *Adv. Mater.* **2018**, *30*, 1703725.
- [21] C. Xia, J. Guo, P. Li, X. Zhang, H. N. Alshareef, *Angew. Chem. Int. Ed.* **2018**, *57*, 3943–3948.
- [22] C. Liu, Z. Neale, J. Zheng, X. Jia, J. Huang, M. Yan, M. Tian, M. Wang, J. Yang, G. Cao, *Energy Environ. Sci.* **2019**, 19–21.

- [23] Y. Yang, Y. Tang, S. Liang, Z. Wu, G. Fang, X. Cao, C. Wang, T. Lin, A. Pan, J. Zhou, *Nano Energy* **2019**, *61*, 617–625.
- [24] Y. Oka, T. Yao, *J. Solid State Chem.* **1997**, *329*, 323–329.
- [25] Y. Oka, O. Tamada, T. Yao, N. Yamamoto, *J. Solid State Chem.* **1996**, *126*, 65–73.
- [26] P. Y. Zavalij, M. S. Whittingham, *Acta Crystallogr. Sect. B Struct. Sci.* **1999**, *55*, 627–663.
- [27] P. M. Marley, S. Banerjee, *Inorg. Chem.* **2012**, *51*, 5264–5269.
- [28] H. Katzke, W. Depmeier, *Phase Transitions* **1996**, *59*, 91–104.
- [29] C. Sun, S. Rajasekhara, J. B. Goodenough, F. Zhou, *J. Am. Chem. Soc.* **2011**, *133*, 2132–2135.
- [30] T. Jiang, F. Bu, X. Feng, I. Shakir, G. Hao, Y. Xu, *ACS Nano* **2017**, *11*, 5140–5147.
- [31] K. X. Wang, X. H. Li, J. S. Chen, *Adv. Mater.* **2015**, *27*, 527–545.
- [32] C. Yan, G. Chen, X. Zhou, J. Sun, C. Lv, *Adv. Funct. Mater.* **2016**, *26*, 1428–1436.
- [33] C. K. Tsung, J. Fan, N. Zheng, Q. Shi, A. J. Forman, J. Wang, G. D. Stucky, *Angew. Chem. Int. Ed.* **2008**, *47*, 8682–8686.
- [34] J. L. Andrews, S. Singh, C. Kilcoyne, P. J. Shamberger, G. Sambandamurthy, S. Banerjee, *MRS Commun.* **2017**, *7*, 634–641.
- [35] L. Abello, E. Husson, Y. Repelin, G. Lucazeau, *Spectrochim. Acta Part A Mol. Spectrosc.* **1983**, *39*, 641–651.
- [36] B. Yan, L. Liao, Y. You, X. Xu, Z. Zheng, Z. Shen, J. Ma, L. Tong, T. Yu, *Adv. Mater.* **2009**, *21*, 2436–2440.
- [37] R. Baddour-Hadjean, M. B. Smirnov, K. S. Smirnov, V. Y. Kazimirov, J. M. Gallardo-Amores, U. Amador, M. E. Arroyo-De Dompablo, J. P. Pereira-Ramos, *Inorg. Chem.* **2012**, *51*, 3194–3201.
- [38] C. Julien, J. P. Guesdon, A. Gorenstein, A. Khelifa, I. Ivanov, *Appl. Surf. Sci.* **1995**, *90*, 389–391.
- [39] R. Manikandan, C. Justin Raj, M. Rajesh, B. C. Kim, S. Y. Park, B. B. Cho, K. H. Yu, *Electrochim. Acta* **2017**, *230*, 492–500.
- [40] D. Vernardou, E. Spanakis, G. Kenanakis, E. Koudoumas, N. Katsarakis, *Mater. Chem. Phys.* **2010**, *124*, 319–322.
- [41] R. Baddour-Hadjean, E. Raekelboom, J. P. Pereira-Ramos, *Chem. Mater.* **2006**, *18*, 3548–3556.
- [42] S. I. Cordoba-Torresi, A. Hugot-Le Goff, S. Joiret, *J. Electrochem. Soc.* **1991**, *138*, 1554–1559.

- [43] B. B. Li, X. Q. Xiu, R. Zhang, Z. K. Tao, L. Chen, Z. L. Xie, Y. D. Zheng, Z. Xie, *Mater. Sci. Semicond. Process.* **2006**, *9*, 141–145.
- [44] Y. Xu, H. Dong, M. Zhou, C. Zhang, Y. Wu, W. Li, Y. Dong, Y. Lei, *Small Methods* **2018**, 1800349.
- [45] C. Tripon, D. Toloman, M. Aluas, C. Filip, I. Ardelean, *J. Optoelectron. Adv. Mater.* **2006**, *8*, 1129–1131.
- [46] Y. Liu, B. Shen, X. Liu, Y. Wu, X. He, Q. Li, *Int. J. Electrochem. Sci.* **2017**, *12*, 5483–5491.
- [47] M. Xue, J. Ge, H. Zhang, J. Shen, *Appl. Catal. A Gen.* **2007**, *330*, 117–126.
- [48] B. Tang, G. Fang, J. Zhou, L. Wang, Y. Lei, C. Wang, T. Lin, Y. Tang, S. Liang, *Nano Energy* **2018**, *51*, 579–587.
- [49] B. Tang, J. Zhou, G. Fang, F. Liu, C. Zhu, C. Wang, A. Pan, S. Liang, *J. Mater. Chem. A* **2019**, *7*, 940–945.
- [50] Y. Yang, Y. Tang, G. Fang, L. Shan, J. Guo, W. Zhang, C. Wang, L. Wang, J. Zhou, S. Liang, *Energy Environ. Sci.* **2018**, *11*, 3157–3162.
- [51] K. Lu, Z. Hu, Z. Xiang, J. Ma, B. Song, J. Zhang, H. Ma, *Angew. Chem. Int. Ed.* **2016**, *55*, 10448–10452.
- [52] Y. Oka, T. Yao, N. Yamamoto, *J. Solid State Chem.* **1990**, *89*, 372–377.
- [53] J. Shin, D. S. Choi, H. J. Lee, Y. Jung, J. W. Choi, *Adv. Energy Mater.* **2019**, *9*, 1900083.
- [54] S. Slam, M. H. Alfaruqi, D. Y. Putro, V. Soundharrajan, B. Sambandam, J. Jo, S. Park, S. Lee, V. Mathew, J. Kim, *J. Mater. Chem. A* **2019**, *7*, 20335–20347.
- [55] B. Tang, J. Zhou, G. Fang, S. Guo, X. Guo, L. Shan, Y. Tang, S. Liang, *J. Electrochem. Soc.* **2019**, *166*, 480–486.
- [56] L. Shan, Y. Yang, W. Zhang, H. Chen, G. Fang, J. Zhou, S. Liang, *Energy Storage Mater.* **2019**, *18*, 10–14.
- [57] M. Morcrette, P. Rozier, L. Dupont, E. Mugnier, L. Sannier, J. Galy, J. M. Tarascon, *Nat. Mater.* **2003**, *2*, 755–761.
- [58] K. Kirshenbaum, D. C. Bock, C. Lee, Z. Zhong, K. J. Takeuchi, A. C. Marschilok, E. S. Takeuchi, *Science* **2015**, *347*, 149–154.
- [59] V. Bodenez, L. Dupont, M. Morcrette, C. Surcin, D. W. Murphy, J. M. Tarascon, *Chem. Mater.* **2006**, *18*, 4278–4287.

- [60] P. Hu, T. Zhu, X. Wang, X. Wei, M. Yan, J. Li, W. Luo, W. Yang, W. Zhang, L. Zhou, Z. Zhou, L. Mai, *Nano Lett.* **2018**, *18*, 1758–1763.
- [61] M. Yan, P. He, Y. Chen, S. Wang, Q. Wei, K. Zhao, X. Xu, Q. An, Y. Shuang, Y. Shao, K. T. Mueller, L. Mai, J. Liu, J. Yang, *Adv. Mater.* **2018**, *30*, 1703725.
- [62] R. Baddour-Hadjean, C. Navone, J. P. Pereira-Ramos, *Electrochim. Acta* **2009**, *54*, 6674–6679.
- [63] D. Asakura, E. Hosono, Y. Nanba, H. S. Zhou, J. Okabayashi, C. M. Ban, P. A. Glans, J. H. Guo, T. Mizokawa, G. Chen, A. J. Achkar, D. G. Hawthorn, T. Z. Regier, H. Wadati, *Aip Adv.* **2016**, *6*, 035105.
- [64] W. W. Gu, H. X. Wang, K. Wang, *Dalton Trans.* **2014**, *43*, 6406–6413.
- [65] F. M. F. Degroot, *J. Electron Spectrosc. Relat. Phenom.* **1994**, *67*, 529–622.
- [66] J. Vanelp, B. G. Searle, G. A. Sawatzky, M. Sacchi, *Solid State Commun.* **1991**, *80*, 67–71.
- [67] G. Ghiringhelli, A. Piazzalunga, C. Dallera, T. Schmitt, V. N. Strocov, J. Schlappa, L. Patthey, X. Wang, H. Berger, M. Grioni, *Phys. Rev. Lett.* **2009**, *102*, 027401.
- [68] G. Vanderlaan, J. Zaanen, G. A. Sawatzky, R. Karnatak, J. M. Esteva, *Phys. Rev. B* **1986**, *33*, 4253–4263.
- [69] J. Jeong, K. J. Park, E. J. Cho, H. J. Noh, S. B. Kim, H. D. Kim, *J Korean Phys. Soc.* **2018**, *72*, 111–115.
- [70] S. Lee, T. L. Meyer, C. Sohn, D. Lee, J. Nichols, D. Lee, S. S. A. Seo, J. W. Freeland, T. W. Noh, H. N. Lee, *APL Mater.* **2015**, *3*, 126109.
- [71] C. L. Chen, C. L. Dong, Y. K. Ho, C. C. Chang, D. H. Wei, T. C. Chan, J. L. Chen, W. L. Jang, C. C. Hsu, K. Kumar, M. K. Wu, *Europhys. Lett.* **2013**, *101*, 17006.
- [72] D. Maganas, M. Roemelt, M. Havecker, A. Trunschke, A. Knop-Gericke, R. Schlogl, F. Neese, *Phys. Chem. Chem. Phys.* **2013**, *15*, 7260–7276.
- [73] D. Maganas, M. Roemelt, T. Weyhermuller, R. Blume, M. Havecker, A. Knop-Gericke, S. DeBeer, R. Schlogl, F. Neese, *Phys. Chem. Chem. Phys.* **2014**, *16*, 264–276.
- [74] R. J. O. Mossaneck, A. Mocellin, M. Abbate, B. G. Searle, P. T. Fonseca, E. Morikawa, *Phys. Rev. B* **2008**, *77*, 075118.
- [75] D. K. Bora, X. Cheng, M. Kapilashrami, P. A. Glans, Y. Luo, J. H. Guo, *J. Synchrotron Rad.* **2015**, *22*, 1450–1458.
- [76] L. Lukashuk, N. Yigit, H. Li, J. Bernardi, K. Föttinger, G. Rupprechter, *Catal. Today* **2019**, *336*, 139–147.

- [77] S. Y. Istomin, O. A. Tyablikov, S. M. Kazakov, E. V. Antipov, A. I. Kurbakov, A. A. Tsirlin, N. Hollmann, Y. Y. Chin, H. J. Lin, C. T. Chen, A. Tanaka, L. H. Tjeng, Z. Hu, *Dalton Trans.* **2015**, *44*, 10708-10713.
- [78] R. Dovesi, A. Erba, R. Orlando, C. M. Zicovich-Wilson, B. Civalleri, L. Maschio, M. Rérat, S. Casassa, J. Baima, S. Salustro, B. Kirtman, *Wiley Interdiscip. Rev. Comput. Mol. Sci.* **2018**, *8*, 1–36.
- [79] T. Wu, K. Zhu, C. Qin, K. Huang, *J. Mater. Chem. A* **2019**, *7*, 5612-5620.
- [80] K. McColl, F. Corà, *J. Mater. Chem. A* **2019**, *7*, 3704–3713.
- [81] J. Livage, P. Barboux, J. C. Badot, N. Baffier, *MRS Proc.* **1988**, *121*, 167.
- [82] S. R. Daemi, C. Tan, T. Volkenandt, S. J. Cooper, A. Palacios-Padros, J. Cookson, D. J. L. Brett, P. R. Shearing, *ACS Appl. Energy Mater.* **2018**, *1*, 3702–3710.

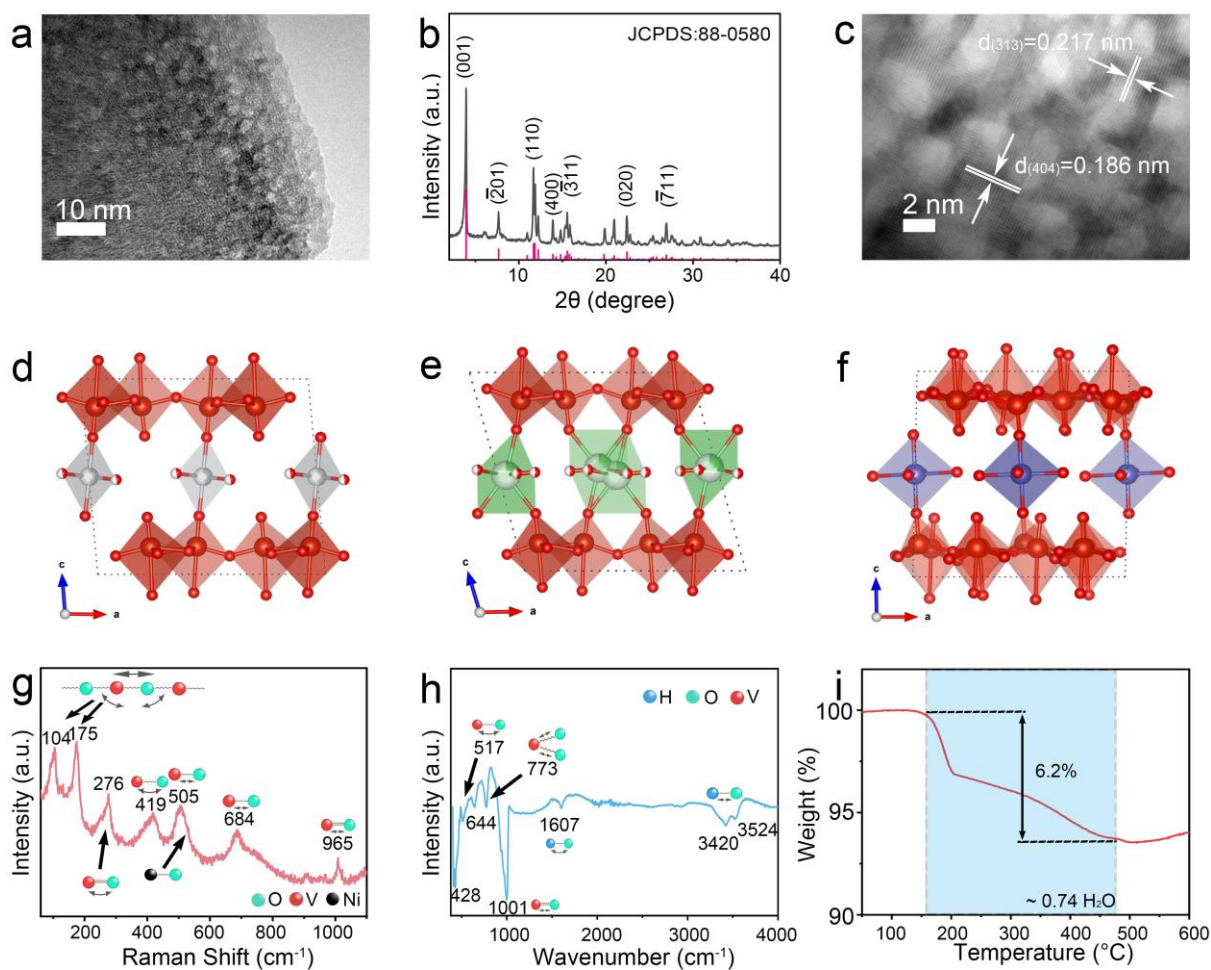


Figure 1. (a) TEM; (b) XRD pattern; (c) HRTEM of as-obtained $\text{Ni}_{0.25}\text{V}_2\text{O}_5 \cdot n\text{H}_2\text{O}$; (d), (e), (f) crystallographic structure of $\delta\text{-Ni}_{0.25}\text{V}_2\text{O}_5 \cdot n\text{H}_2\text{O}$, $\delta\text{-Ca}_{0.25}\text{V}_2\text{O}_5 \cdot n\text{H}_2\text{O}$ ^[21] and $\sigma\text{-Zn}_{0.25}\text{V}_2\text{O}_5 \cdot n\text{H}_2\text{O}$ ^[17] projected along the b -axis, respectively. Ni atoms are grey, Ca green and Zn blue. V atoms are large red spheres and O atoms are small red spheres. Shaded regions indicate coordination polyhedra, and partially filled spheres indicate fractionally occupied sites; (g) Raman spectrum; (h) FTIR spectrum and (i) TGA results of the $\text{Ni}_{0.25}\text{V}_2\text{O}_5 \cdot n\text{H}_2\text{O}$.

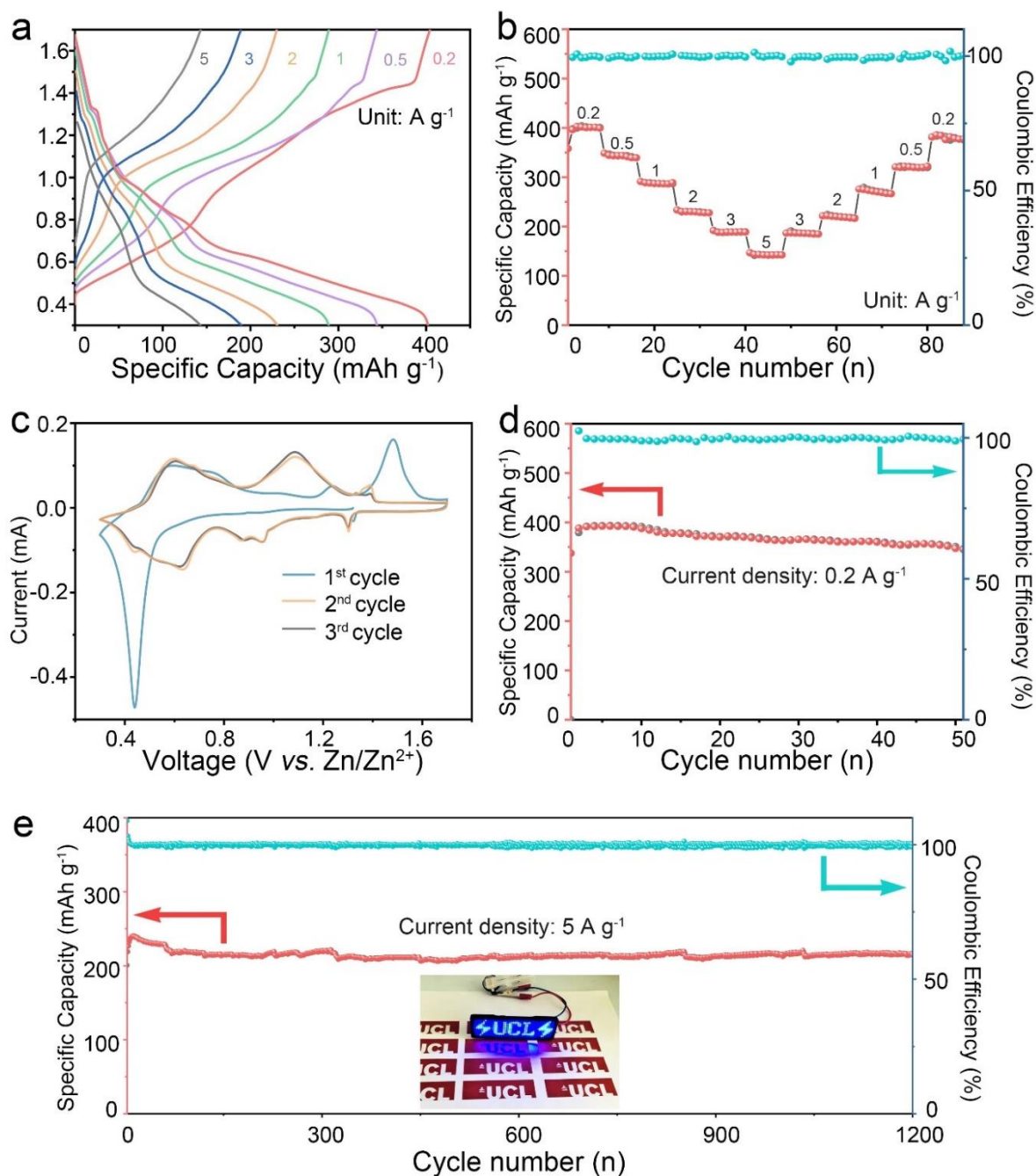


Figure 2. (a) Galvanostatic charge-discharge profiles for $\text{Ni}_{0.25}\text{V}_2\text{O}_5 \cdot n\text{H}_2\text{O}$ cathodes at different current densities; (b) Rate performance of $\text{Ni}_{0.25}\text{V}_2\text{O}_5 \cdot n\text{H}_2\text{O} // \text{Zn}$ batteries; (c) Cyclic voltammetry curves of $\text{Ni}_{0.25}\text{V}_2\text{O}_5 \cdot n\text{H}_2\text{O}$ electrodes at the scan rate of 0.2 mV s^{-1} for the first three cycles; Stability evaluation of $\text{Ni}_{0.25}\text{V}_2\text{O}_5 \cdot n\text{H}_2\text{O}$ at current densities of (d) 0.2 and (e) 5 A g^{-1} , respectively. Inset in e showing the as-assembled batteries lightening the LED logos.

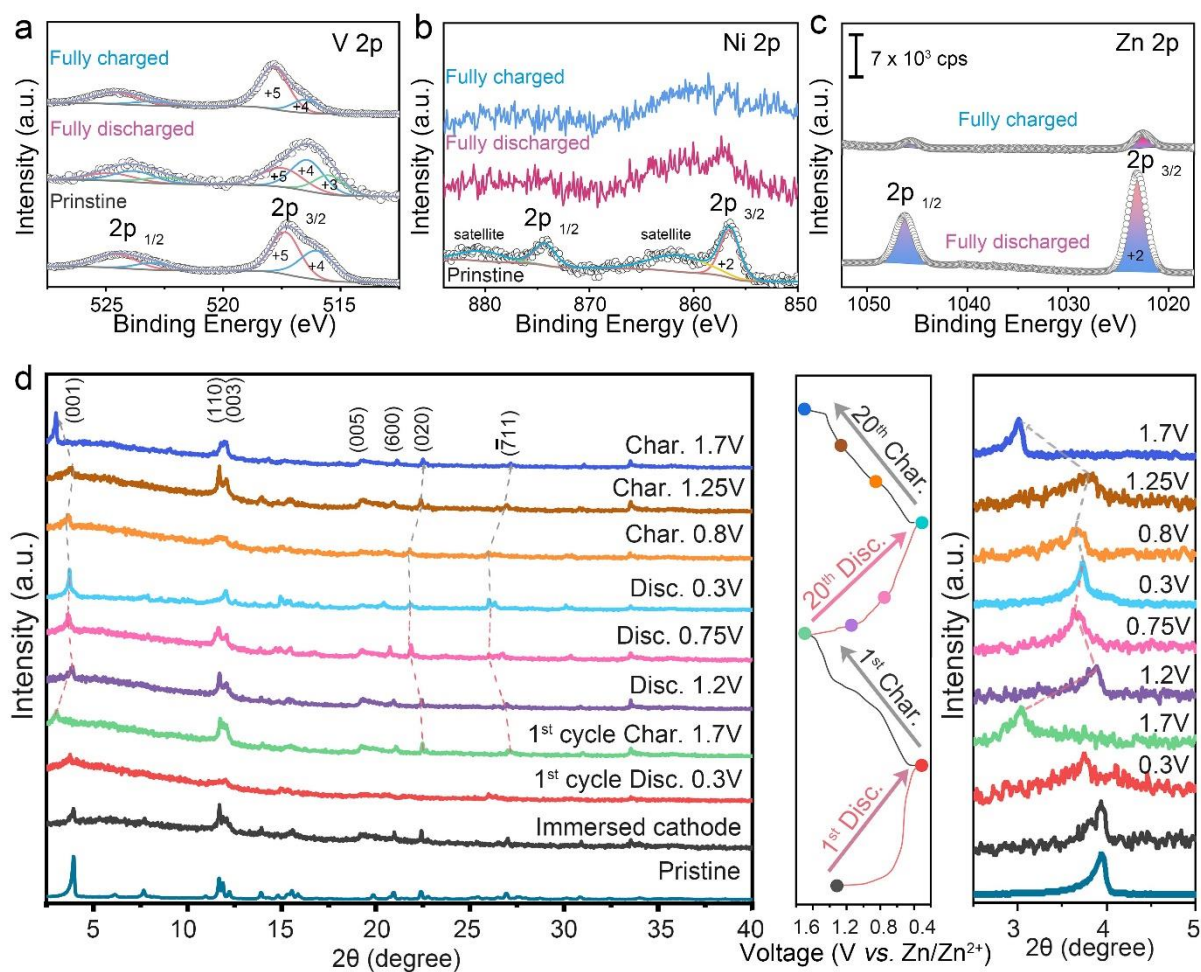


Figure 3. *Ex-situ* XPS spectra of the (a) V 2p, (b) Ni 2p and (c) Zn 2p regions in pristine, fully charged and fully discharged states of the $\text{Ni}_{0.25}\text{V}_2\text{O}_5 \cdot n\text{H}_2\text{O}$ cathodes, respectively; (d) *Ex-situ* XRD characterization of the $\text{Ni}_{0.25}\text{V}_2\text{O}_5 \cdot n\text{H}_2\text{O}$ cathodes upon charge-discharge processes and its corresponding galvanostatic charge-discharge profiles at the current density of 0.2 A g^{-1} .

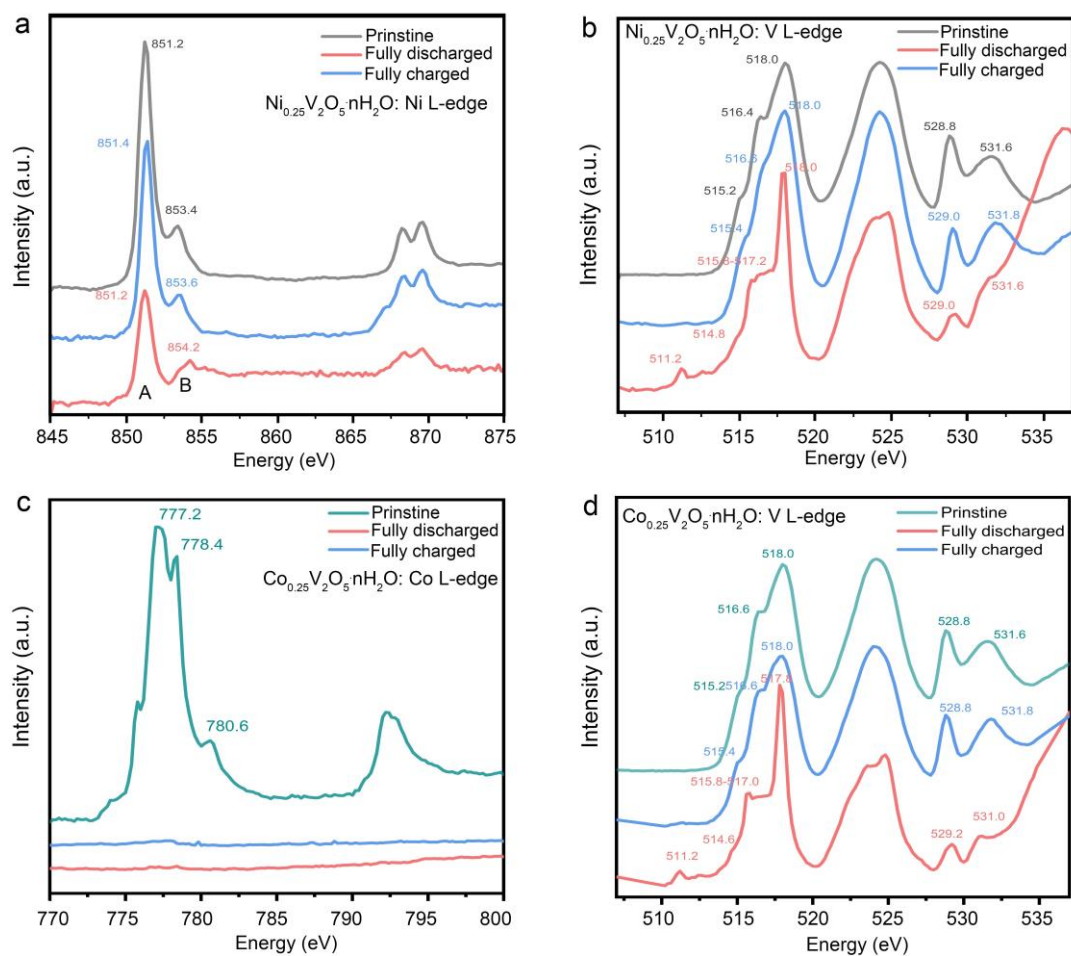


Figure 4. (a) Ni and (b) V L-edge NEXAFS spectra of fresh, 20th cycles discharged and 20th cycles charged Ni_{0.25}V₂O₅·nH₂O, respectively. (c) Co and (d) V L-edge NEXAFS spectra of fresh, 20th cycles discharged and 20th cycles charged Co_{0.25}V₂O₅·nH₂O, respectively.

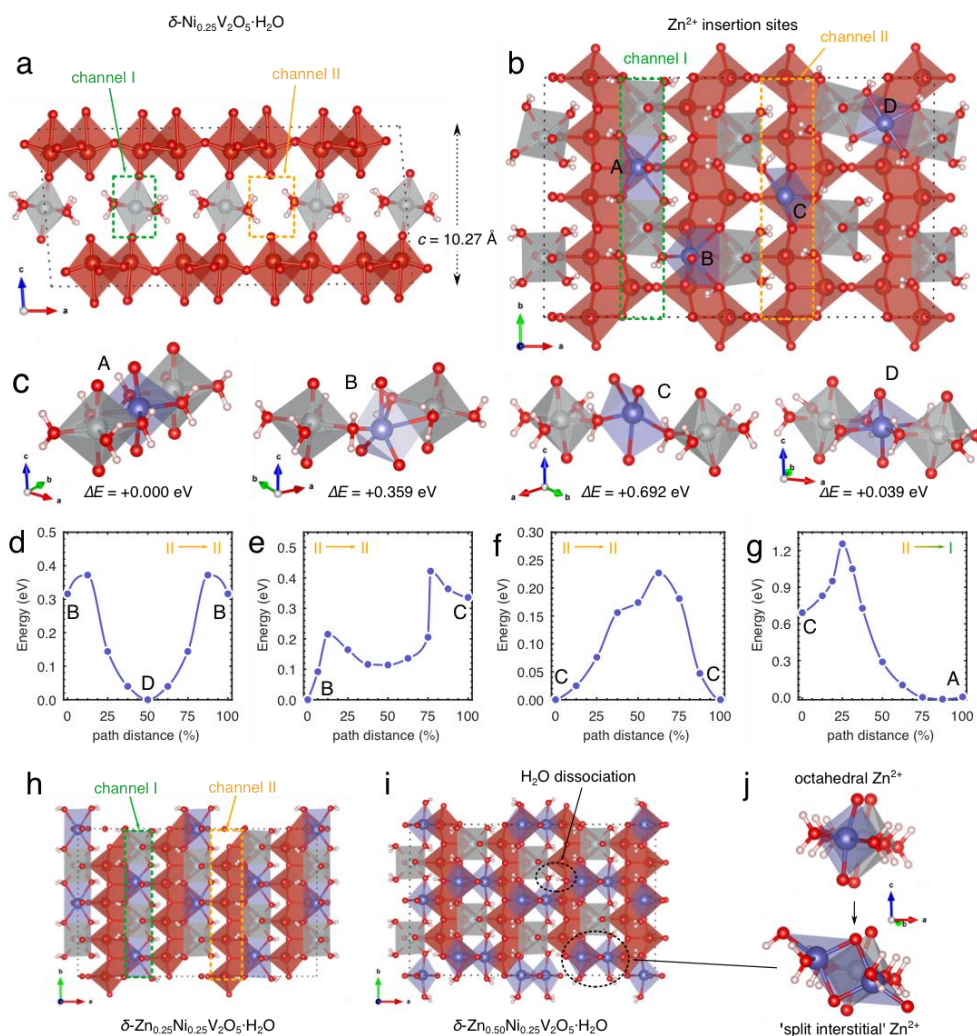


Figure 5. (a) B3LYP-D3 calculated structure of Ni_{0.25}V₂O₅·H₂O, highlighting channels I and II. V ions are large red spheres, Ni ions are grey spheres and O ions are small red spheres, Shaded regions illustrate cation coordination polyhedra; (b) Intercalation sites A, B, C and D for Zn²⁺ ions at a stoichiometry of Zn_{0.125}Ni_{0.25}V₂O₅·H₂O. Zn ions are blue spheres. (c) Local geometry and relative energy of sites A – D. (d) – (g) Energy profiles for Zn²⁺ ionic migration between sites. Migration along channel I can occur *via* pathways (d), (e) and (f). Migration from channel II to channel I occurs *via* pathway (g). (h) Stable orderings of Zn²⁺ ions in A sites at a stoichiometry of Zn_{0.25}Ni_{0.25}V₂O₅·H₂O, indicating channel II open for further intercalation. (i) Rearrangement of Zn²⁺ ions and dissociation of some H₂O in Zn_{0.50}Ni_{0.25}V₂O₅·H₂O. (j) Illustration of the transition between octahedral Zn²⁺ and 'split interstitial' Zn²⁺ when stoichiometry of Zn_{0.50}Ni_{0.25}V₂O₅·H₂O is reached.

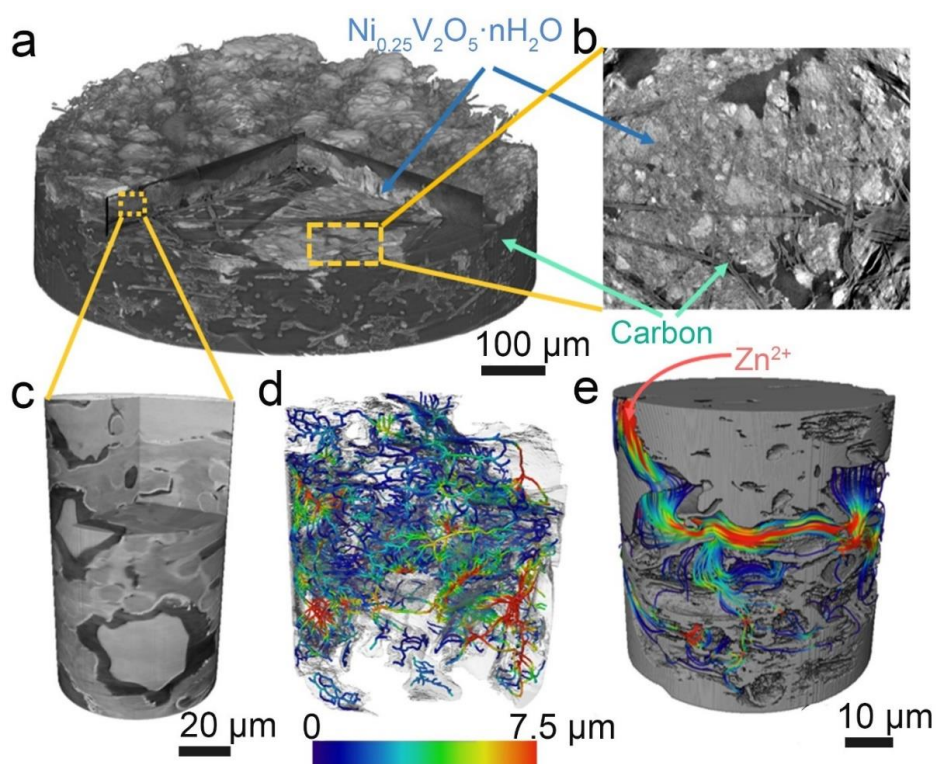


Figure 6. Multi-length scale visualisation and characterisation of the fabricated $\text{Ni}_{0.25}\text{V}_2\text{O}_5 \cdot n\text{H}_2\text{O}$ electrode. (a) 3D volume rendering of the reconstructed electrode by X-ray micro-CT; (b) virtual slice showing the magnified region in (a); (c) 3D volume rendering of the electrode reconstructed by X-ray nano-CT; (d) skeletonisation of the pore phase with colour showing the local pore size distribution; (e) streamlines showing the flux distribution in diffusion simulation based on the reconstructed pore morphology.

The table of contents entry

The synthesis of δ -Ni_{0.25}V₂O₅ materials were reported as aqueous Zinc-ion batteries cathodes, the materials and electrodes were undergone from molecular, nanoscale to microscopic scale investigation. The cathode material shows best in class capacity (402 mAh g⁻¹ at 0.2 A g⁻¹) and stability (a capacity retention of 98 % over 1200 cycles at 5 A g⁻¹).

Keywords Zn-ion battery, cathode, DFT calculation, 3D tomography

Jianwei Li, Kit McColl, Xuekun Lu, Sanjayan Sathasivam, Haobo Dong, Liqun Kang, Zhuangnan Li, Siyu Zhao, Andreas G. Kafizas, Ryan Wang, Dan J. L. Brett, Paul R. Shearing, Furio Corà, Guanjie He*, Claire J. Carmalt and Ivan P. Parkin*

Title

Multi-scale Investigation of δ -Ni_{0.25}V₂O₅ Cathode Materials in Aqueous Zinc-ion Batteries

ToC figure

